Article

Characterization of Irradiated Boron, Carbon-Enriched and Gallium Si-on-Si Wafer Low Gain Avalanche Detectors

Lucía Castillo García [1,*], Evangelos Leonidas Gkougkousis [2], Chiara Grieco [1] and Sebastian Grinstein [1,3]

[1] Institut de Física d'Altes Energies (IFAE), The Barcelona Institute of Science and Technology (BIST), Carrer Can Magrans s/n, Edifici Cn, Campus UAB, E-08193 Barcelona, Spain; chiara.grieco@cern.ch (C.G.); sgrinstein@ifae.es (S.G.)

[2] Conseil Européen pour la Recherche Nucléaire (CERN), EP Department, Esplanade des Particules 1, CH-1211 Geneva 23, Switzerland; vagelis.gkougkousis@cern.ch

[3] Institució Catalana de Recerca i Estudis Avançats (ICREA), Passeig de Lluís Companys, E-08010 Barcelona, Spain

[*] Correspondence: lucia.castillo.garcia@cern.ch

Abstract: Low Gain Avalanche Detectors (LGADs) are n-on-p silicon sensors with an extra doped p-layer below the n-p junction which provides signal amplification. The moderate gain of these sensors, together with the relatively thin active region, provides excellent timing performance for Minimum Ionizing Particles (MIPs). To mitigate the effect of pile-up during the High-Luminosity Large Hadron Collider (HL-LHC) era, both ATLAS and CMS experiments will install new detectors, the High-Granularity Timing Detector (HGTD) and the End-Cap Timing Layer (ETL), that rely on the LGAD technology. A full characterization of LGAD sensors fabricated by Centro Nacional de Microelectrónica (CNM), before and after neutron irradiation up to 10^{15} n_{eq}/cm^2, is presented. Sensors produced in 100 mm Si-on-Si wafers and doped with boron and gallium, and also enriched with carbon, are studied. The results include their electrical characterization (I-V, C-V), bias voltage stability and performance studies with the Transient Current Technique (TCT) and a Sr-90 radioactive source setup.

Keywords: LGAD; timing detectors; silicon sensors

1. Introduction

The Large Hadron Collider (LHC), located at CERN, is the world's most powerful particle accelerator. By studying the hadron collisions at the LHC, various experiments probe our understanding of the fundamental particles and their interactions. To increase its physics reach, the LHC will be improved to be able to achieve about seven times the current instantaneous luminosity. The High-Luminosity LHC (HL-LHC) [1,2] is currently foreseen to start operations in 2027.

The expected increase in instantaneous luminosity during the HL-LHC era will result in a high-multiplicity environment for both ATLAS and CMS experiments [3,4]. In addition, the targeted total luminosity of 4000 fb^{-1} imposes extreme radiation hardness constraints. For each collision, within a 150 ps time frame and at 50 mm space, an average number of pile-up interactions of 200 is estimated. At the HL-LHC end of life, a total dose of about 10^{16} n_{eq}/cm^2 is expected for the inner most layer of the ATLAS tracking detector (ITk) [5]. Though the ITk detector will provide excellent position resolution, its performance degrades towards the forward region [5]. Maintaining vertex separation in such a demanding environment while achieving the pile-up rejection level required for photon and lepton identification and jet tagging performance at high $|\eta|$ will not be possible using only position information. The addition of 50 ps per track timing information can mitigate the performance degradation to manageable (Run 1) levels. The need for a fast, compact radiation hard segmented sensor adapted to the next generation of particle physics experiments becomes apparent [6]. The recently developed Low Gain Avalanche Detector

(LGAD) [7] technology has been investigated by the LHC experiments as a solution to cope with the increased pile-up of the high-luminosity era. Both ATLAS and CMS experiments plan to install detectors based on LGADs in 2025, the High-Granularity Timing Detector (HGTD) [8] and the End-Cap Timing Layer (ETL) [9], respectively.

In a slightly different approach, the LHCb collaboration is also considering the use of precise timing information for primary vertex (PV) assignation. In spite of the lower expected pile-up ($\sim$50), because of the long-lived heavy particle-focused physics program, an extremely precise association of each candidate to its original PV is required. It is estimated that the addition of 100 ps timing information will reduce PV misassociation rate to 4% from the 22% otherwise projected for LHC-Phase 2 [10].

In this paper, the stability and performance of proton and neutron irradiated LGAD sensors up to fluences of 10^{15} n_{eq}/cm^2 is discussed. The presented results refer exclusively to devices provided by the Centro Nacional de Microelectrónica (CNM) Barcelona using a boron, boron combined with carbon and gallium implantation technology from production runs 10478 and 10924 [11,12].

Previous work on earlier LGAD productions from CNM before and after irradiation are summarized in the following references [13–16]. The LGAD performances were studied using the same experimental setups described in this paper as well as in beam tests.

2. Low Gain Avalache Detectors (LGAD)

LGADs are a technology pioneered by CNM Barcelona and jointly developed during the past five years within the RD50 collaboration [17]. An LGAD consists of a standard n-on-p planar silicon diode with the addition of a highly doped p-layer under the collection electrode (multiplication layer). The latter introduces an area with a strong electric field, resulting in the acceleration of drifting charge carriers towards the anode. Field values in excess of the 20 V/µm impact ionization threshold [7] are observed within the gain layer in a relatively small volume of a few microns. Charge multiplication of the initial charge deposited within the sensor bulk can thus be achieved. Typical gain layer implants may include any acceptor type element commonly used in semiconductor fabrication, including most commonly boron, gallium, aluminum, indium etc. Additional non-electrically active implants may be added for post-irradiation performance optimization. Such elements may include carbon and/or oxygen.

Samples

All of the subsequent studies were performed on single pad sensors comprised of a 1.0×1.0 mm^2 active area surrounded by a single guard ring on a 2.0×2.0 mm^2 die. A schematic cross section of the devices is presented in Figure 1. A 0.7×0.7 mm^2 gain layer and n-type collection electrode are centered within the pad region, encircled by a deeper secondary n-implant. The latter, known as the Junction Termination Extension (JTE), mitigates high field values created by sharp geometrical structures at the edge and provides electrical isolation between the central region and the guard ring. For a first approximation, the JTE and guard ring implants can be equally treated while the addition of a p-stop layer between the two reduces charges sharing between the structures. Although a charge collected at the JTE region does not usually undergo multiplication, it is still collected via the top metallization layer. A uniform p-implant is implemented on the sensor backside spanning the entire die.

An active thickness of 50 µm was chosen on a 300 µm carrier, using a wafer-to-wafer bonding process. Access to the cathode electrode is achieved by etching the support wafer until the ohmic contact is reached. A metal layer is then deposited to cover the backside.

As an implant for the multiplication layer, boron (wafer 4, dose 1.5×10^{13} atoms/cm^2) is used. As an alternative, carbon spray (wafer 5) and gallium implant (wafer 6, dose 6×10^{13} atoms/cm^2) are also investigated as possible candidates for improving the radiation hardness. In the case of boron plus carbon LGADs, the carbon was implanted with a spray applied on top of the entire wafer at the beginning of the process. The thermal steps

are the same for all the wafers. The JTE is made of phosphorus while the p-stop is boron for the wafers with gallium.
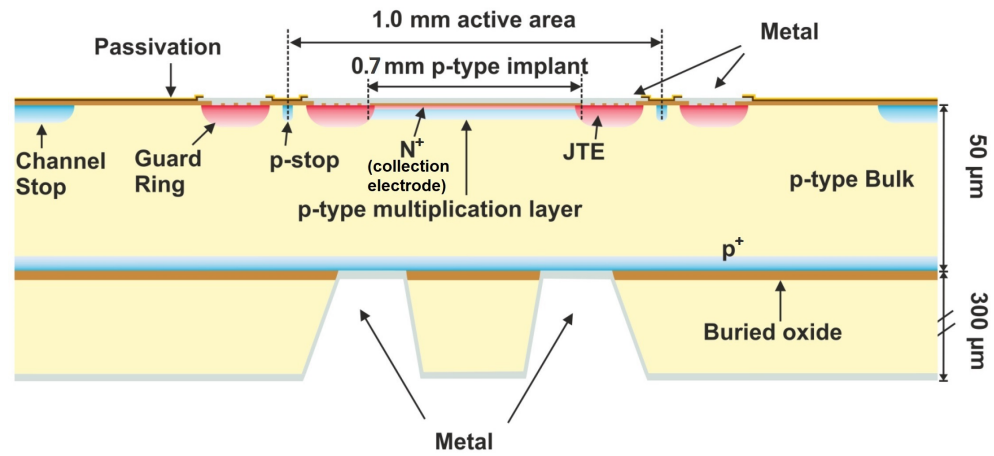

Figure 1. Cross section of a single pad LGAD diode structure.

The irradiation campaigns took place at two facilities with different particle types and energies: the Jožef Stefan Institute, Ljubljana (1 MeV neutrons) and the CERN Proton Synchrotron (23 GeV protons). Table 1 shows the list of tested sensors.

Table 1. List of tested CNM devices with different implants (boron, boron plus carbon and gallium) irradiated up to 10^{15} n_{eq}/cm^2.

Run	Wafer	Implant	Un-Irrad	10^{14} n_{eq}/cm^2	6×10^{14} n_{eq}/cm^2	10^{15} n_{eq}/cm^2	Irradiation Type
10478	W4	Boron	S1022	S1095 S1067	S1016 S1064	S1068	neutron proton
	W5	Boron+ C-enriched	S1013	S1005 S1038	S1008 S1076	S1009	neutron proton
10924	W6	Gallium	S1021	S1007 S1023	S1012 S1036	S1009	neutron proton

3. Electrical Characterization

Initially, each device was pre-characterized at the producer site where capacitance-voltage (C-V) measurements at room temperature were performed before irradiation [12]. Many unirradiated samples of each type were tested including those listed in Table 1. As shown in Figure 2, in the case of boron and boron plus carbon, the gain layer voltage, V_{gl}, is about 38 V and the full depletion voltage, V_{fd}, about 42 V, whereas for the gallium samples V_{gl} = 32 V to 64 V and V_{fd} = 40 V to 80 V. This variation in V_{gl} is explained by the fact that gallium penetrates less than boron in silicon because the atoms are bigger and during the annealing it diffuses faster than boron. The higher the full depletion voltage is, the smaller the room to operate the device before irradiation at −30 °C. PIN diodes were also fabricated in the same process run as the LGADs but without the multiplication layer. Figure 2a,b show that PINs need less voltage to be depleted.
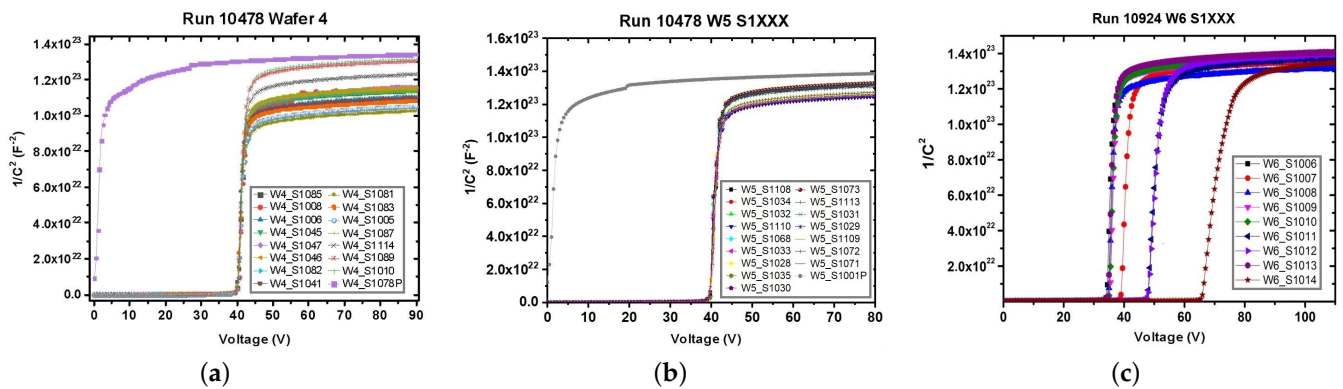
Figure 2. C-V characteristic curves for (**a**) Boron, (**b**) Boron plus Carbon and (**c**) Gallium LGADs performed at room temperature by CNM [12].

The sensors were later characterized on a cooled probe station at $-30\,°C$ in a dry environment. A chiller controller from ATT systems was used (Cooling unit model P10 3060VA polystat CC3). These measurements were performed at the Silicon Laboratory of the Solid State Detector group located at CERN, Switzerland. Figure 3a shows the diagram of the probe station setup where both current-voltage (I-V) and C-V measurements can be performed by selecting the type of measurement via a switch. The equipment required to measure the I-V is a picoammeter whereas for the C-V, it is an LCR meter. Figure 3 shows the experimental setup. Figure 3b shows a picture of the experimental setup. Two needles are available for testing a single pad LGAD, one for the pad and one for the guard ring. The guard ring is connected to the ground. The negative bias voltage is applied from the back of the LGAD through the probe station chuck. The total and the pad currents are measured separately with a sourcemeter (Keithley 2410 1100 V SourceMeter [18]). A LabVIEW-based software is used to control the equipment and acquire the data.
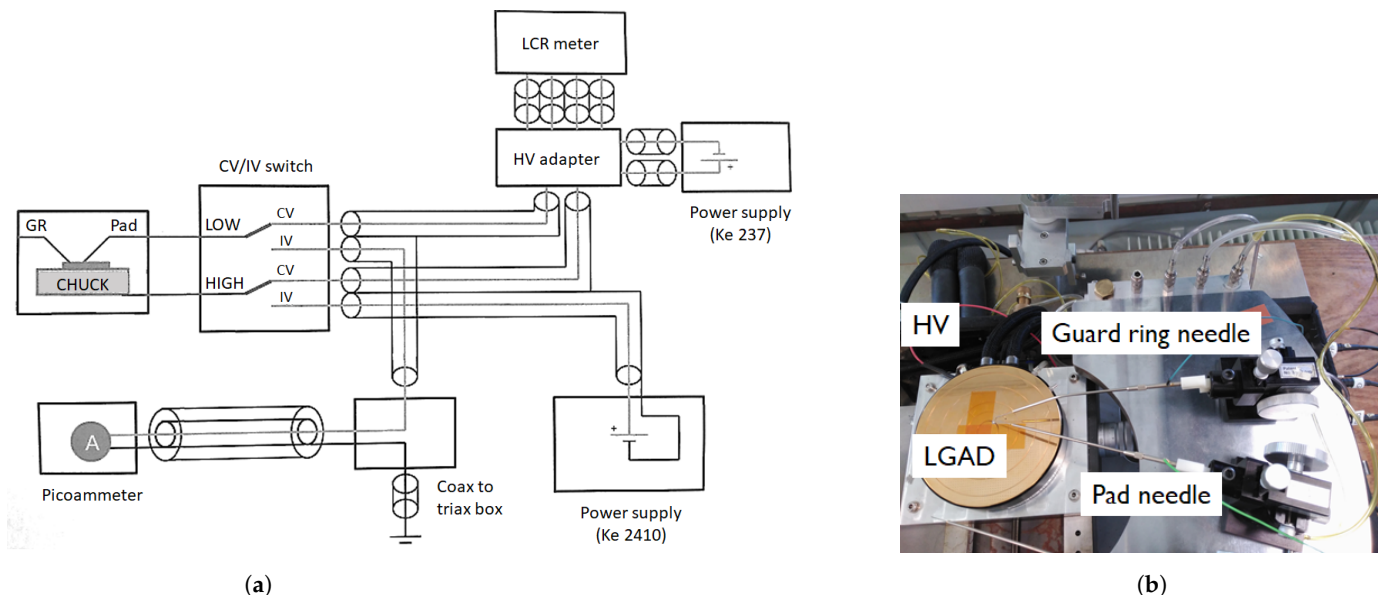

Figure 3. (**a**) I-V/C-V diagram and (**b**) picture of the probe station setup in the Solid State Detectors (SSD) laboratory at CERN.

The leakage current was studied as a function of the bias voltage in order to determine the breakdown voltage, V_{bd}, of each sensor. Figure 4 shows the I-V characteristic curves before and after irradiation. Unirradiated devices have a breakdown at about 130 V (boron), 110 V to 140 V (boron plus carbon) and 140 V (gallium), as seen in Figure A1 in the appendix. The variation in V_{bd} for boron plus carbon devices can be explained by the different position

of the samples in the wafer and possibly related to the carbon spray procedure. The breakdown voltage might differ for sensors located in the central region of the wafer with respect to that for sensors located in the periphery of the wafer. Carbon diffuses a lot and might not be homogeneous through the entire wafer. As expected, it is also observed that the V_{bd} moves towards higher voltages as the irradiation level increases. The breakdown voltage is also shifted towards higher values for proton irradiation with respect to the value for neutron irradiation at the same fluence. The gallium samples have a higher leakage current than the other two types due to the high multiplication and the sensor is close to breakdown once it is depleted.
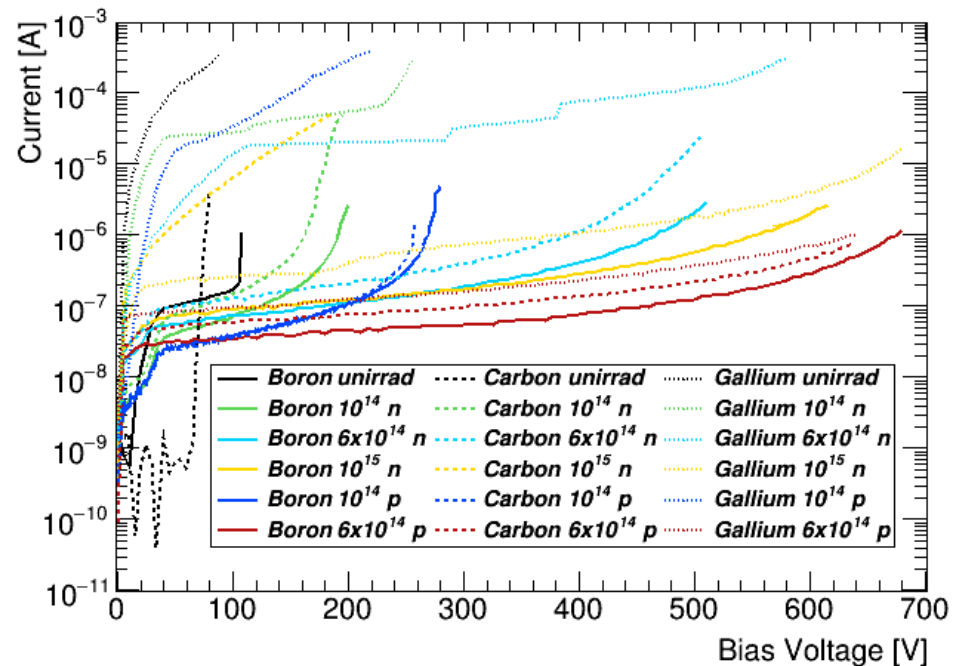

Figure 4. I-V characteristic curves (total = pad + guard ring) before and after three different irradiation levels at $-30\,°C$.

From the I-V curves, one can evaluate the radiation-induced active multiplication implant degradation by looking at its derivative. Using this method, V_{gl} values are obtained and, consequently, by looking at its variation with fluence, the acceptor removal constant is determined for each type of implant. The effective gain can be estimated by comparing the multiplication with the non-multiplication region on the same die looking at the ratio between the pad, I_{pad}, and the guard ring, I_{GR}, currents. The results on these samples using both methods are further discussed in [19,20].

4. Transient Current Technique Measurements

The Transient Current Technique (TCT) [21] consists of measuring time-resolved current waveforms induced by the drift of charges inside a sensor. The current is proportional to the number of charges, to their drift velocity and to the weighting field of the readout electrode. Different detector properties can be determined by the analysis of the recorded waveforms, such as the charge and gain as presented in this paper, the edge size and the inter-pad distance in the case of testing an array of pads. The TCT allows us to perform measurements with good position resolution ($\sim 10\,µm$), allowing us to build a precise two-dimensional map of the LGAD. A pulsed laser source mimics the behavior of charged particles by illuminating the sensor with a large number of photons in a short time interval. An Infra-Red (IR) laser is used because its absorption length in silicon is of the order of millimeters, much larger than the detector thickness (micrometers). In this way, it can simulate the passing of a charged particle. Note, however, that the total charge deposited

by the laser pulse is much larger than the charge corresponding to a Minimum Ionizing Particle (MIP) [22].

4.1. Experimental Setup

The TCT setup at the laboratory of the Institut de Física d'Altes Energies (IFAE), as shown in Figure 5, consists of the following items:

- Two laser sources, Red (660 nm) and Infra-Red (1064 nm);
- An optical system to focus the laser beam;
- A current amplifier (Particulars wide band current amplifier 35 dB);
- A waveform digitizer (A DRS oscilloscope [23]);
- A set of movable stages that allows to move the sensor on the perpendicular plane with respect to the laser beam and along the beam axis;
- A Peltier element and controller to regulate the operational temperature of the device under test (DUT);
- A beam monitor to check the intensity of the laser beam during the measurement;
- A beam splitter serving as an attenuator and transmittin 30% of the incident light to the DUT plane;
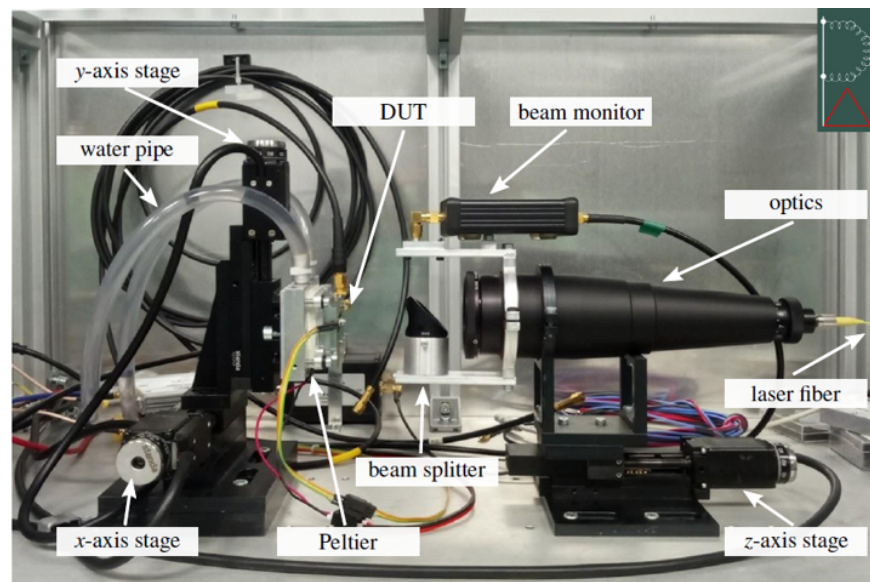- A dry air filter to avoid condensation for measurements at low temperature.

Figure 5. Transient current technique setup.

In order to perform charge collection measurements the sensors were illuminated from the back (ohmic) side, since some of these CNM sensors have an opening in the backside metal specific for TCT measurements. Boron plus carbon devices were full metallized and TCT measurements could not be performed. In Figure 6a, a schematic of the measurement setup is shown. Each sensor is mounted on a metal box as shown in Figure 6b. The sensor pad and guard ring are wire bonded to two different connectors that are connected to a high voltage source and biased with positive voltage. The metal box presents a circular opening to allow us to aim the laser beam to the back of the sensor. The voltage reaches the pad of the sensor through a bias-T element. The signal is obtained through the bias-T, amplified and captured by an oscilloscope which is connected to the Data Acquisition (DAQ) system.
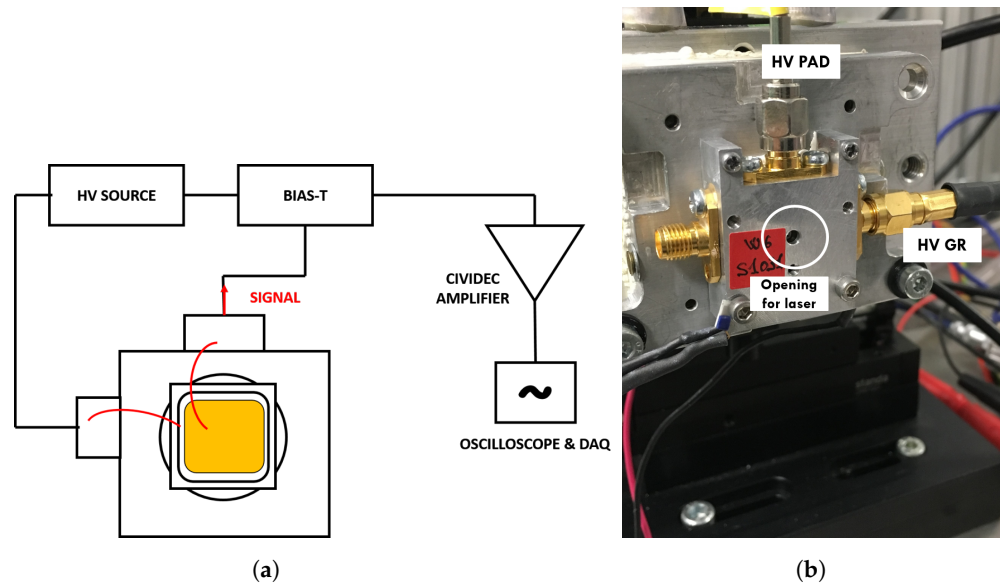
| (**a**) | (**b**) |

Figure 6. (**a**) Sketch of the setup used for the TCT measurements. (**b**) Metal box in which the sensor is located, mounted on the X-Y movable stage.

4.2. Procedure

A set of boron and gallium implanted LGAD sensors irradiated with neutrons and protons up to $10^{15} n_{eq}/\mathrm{cm}^2$, as listed in Table 2, were measured. Boron plus carbon LGADs are fully metallized on the backside and thus it was not possible to measure them. TCT measurements were performed at $-20\,°\mathrm{C}$ in a dry environment. The IR laser was aimed at the center of the back of the sensor to avoid possible edge effects, and the signal induced by the laser pulses was acquired. For each bias voltage value, an average of 300 waveforms was collected. The laser pulse width was set at 60% with a pulse frequency of 200 Hz [15]. The minimum pulse width for this system is 350 ps and the maximum is 4000 ps, where the minimum value corresponds to a pulse width of 100% and the smallest intensity. An example for the recorded waveforms at different bias voltages for an unirradiated LGAD sensor is shown in Figure 7.

Table 2. List of the studied sensors.

| Production Run	Wafer	Sensor	Implant	Fluence [n_{eq}/cm^2]	Irradiation Type	Size
10478	W4	S1022	Boron	Unirradiated	-	$1 \times 1\ \mathrm{mm}^2$
10478	W4	S1067	Boron	10^{14}	proton	$1 \times 1\ \mathrm{mm}^2$
10478	W4	S1095	Boron	10^{14}	neutron	$1 \times 1\ \mathrm{mm}^2$
10478	W4	S1016	Boron	6×10^{14}	neutron	$1 \times 1\ \mathrm{mm}^2$
10478	W4	S1068	Boron	10^{15}	neutron	$1 \times 1\ \mathrm{mm}^2$
10924	W6	S1039P	-	Unirradiated PIN diode	-	$1 \times 1\ \mathrm{mm}^2$
10924	W6	S1041	Gallium	Unirradiated	-	$1 \times 1\ \mathrm{mm}^2$
10924	W6	S1044	Gallium	10^{14}	proton	$1 \times 1\ \mathrm{mm}^2$
10924	W6	S1007	Gallium	10^{14}	neutron	$1 \times 1\ \mathrm{mm}^2$
10924	W6	S1012	Gallium	6×10^{14}	neutron	$1 \times 1\ \mathrm{mm}^2$
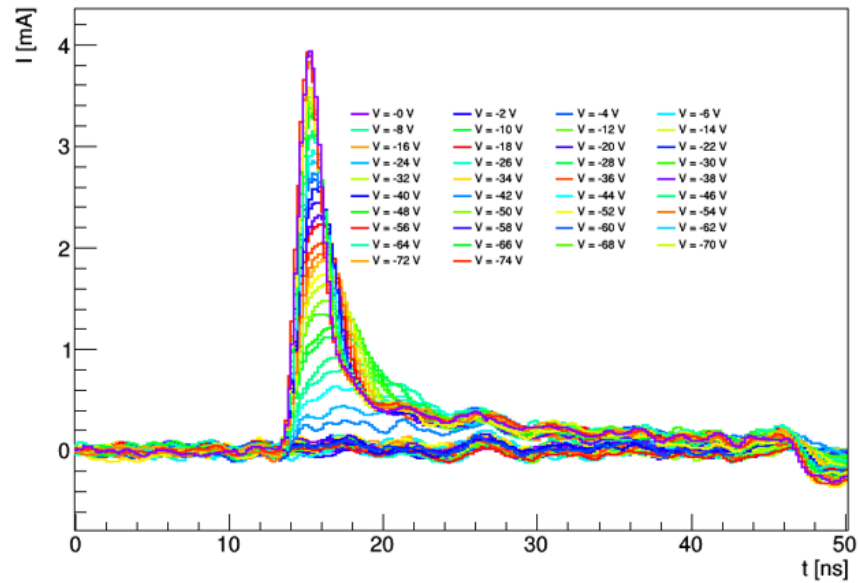
Figure 7. Recorded waveforms at different bias voltages for an unirradiated LGAD.

4.3. Gain

The collected charge is determined from the integral of the waveform around the peak, in the range 12 ns to 24 ns (see Figure 7). In order to calculate the gain, the collected charge at each bias voltage is divided by the average collected charge of a PIN diode:

$$G_i = \frac{Q_i}{< Q_{PIN} >}, \tag{1}$$

The gain values for the different LGADs are shown in Figure 8, where continuous lines correspond to boron sensors and dashed lines correspond to gallium ones. Boron LGADs show a higher gain at the same bias voltage with respect to gallium doped ones. Moreover, proton irradiation presents a higher damage with respect to neutrons at the same fluence.
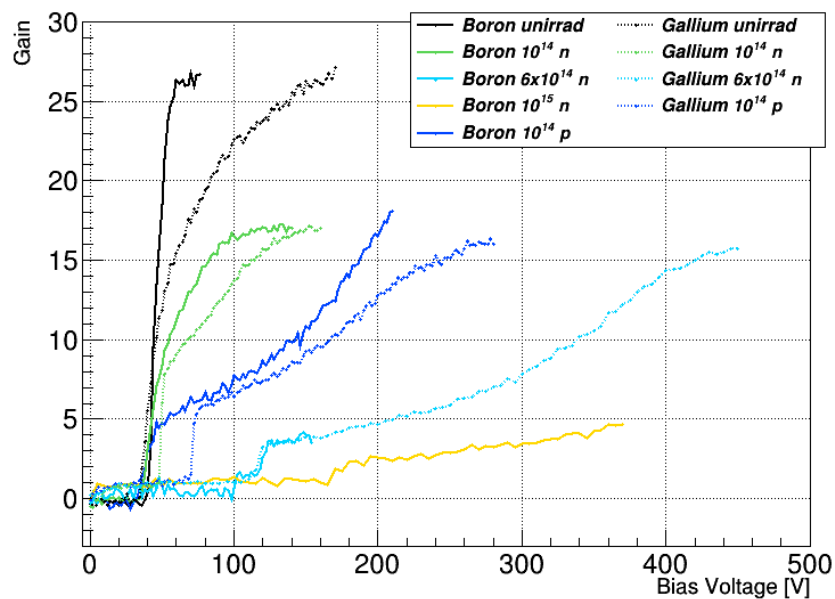

Figure 8. Gain for the boron and gallium CNM LGADs irradiated up to a fluence of 10^{15} n_{eq}/cm^2 at $-20\,°C$.

5. Stability Studies

Sensors with gain present spurious events at high enough voltages. These events are thermally generated and are random in nature. The time between consecutive auto-triggering events when there is no external source is studied using an oscilloscope (LeCroy Waverunner 8104 1 GHz Oscilloscope 20 GS/s [24]). A trigger selection on signals larger than 10 mV equivalent to $\sim 5\sigma_{noise}$ is applied, where the noise level is smaller than 2 mV for all the sensors (see Figure A4). The auto-triggering rate is defined as the inverse of this time difference. Since the waveforms generated by auto-triggering events are identical to the real signal generated by impinging particles, it is critical to measure this rate and operate the sensors below its onset. Figure 9 shows the auto-triggering rate as a function of the bias voltage for the set of tested sensors at $-30\,°C$. No auto-triggering is observed for moderate bias voltages but when the voltage is high enough, the sensors start emitting self-pulses. Unirradiated devices did not present auto-triggering events for the range of voltages they were operated (up to 80 V). Boron plus carbon LGADs auto-trigger at lower voltages than the boron ones and, gallium LGADs auto-trigger at even higher voltages. Samples irradiated with protons at a fluence of 6×10^{14} n_{eq}/cm^2 do not show auto-triggering at any operating voltage. The samples Gallium 10^{14} p and Carbon 10^{15} n could not be operated at higher voltages due to a high current, thus the auto-triggering onset was not measured.
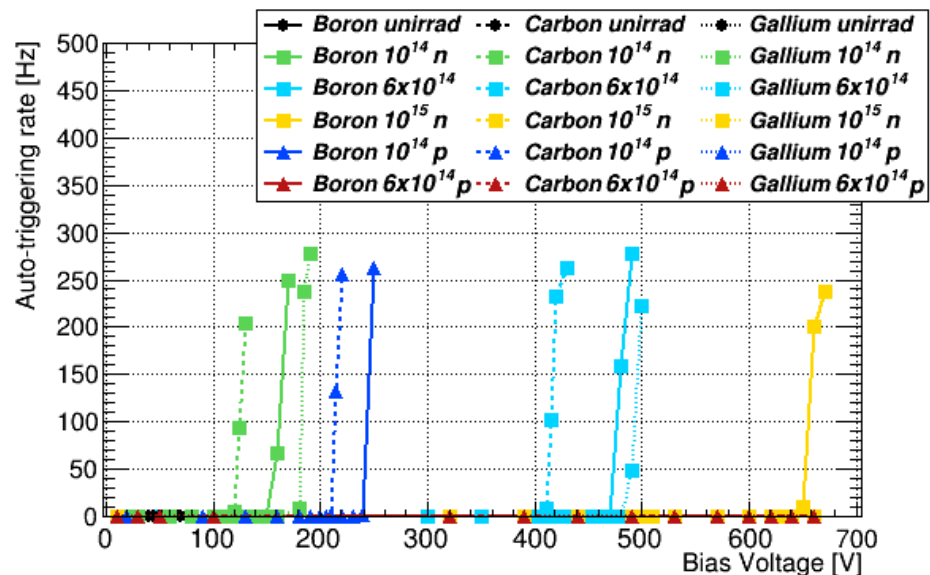

Figure 9. Auto-triggering rate as a function of the bias voltage for CNM LGADs before and after irradiation up to a fluence of 10^{15} n_{eq}/cm^2 at $-30\,°C$.

One factor limiting the operating voltage is the onset of the auto-triggering regime. This limiting value appears before the breakdown voltage. As the gain is reduced in the irradiated samples, the operating point is pushed closer to the breakdown value. The maximum operating voltage with an acceptable auto-triggering rate of 1 kHz is estimated from Figure 9 by extrapolating the measurement to this rate and obtaining the corresponding bias voltage. This limit comes from the average rate of data recorded in ATLAS. An excessive self-triggering would increase the dead time of the HGTD detector hindering its operation. Figure 10 shows the maximum bias voltage for an auto-triggering rate of 1 kHz as a function of fluence. The trend is the same for all three types of implants. Boron and gallium are similar in terms of operational stability. Boron plus carbon features the same level of auto-triggering at less voltage, thus presenting more operational instability. Proton-irradiated samples feature the same auto-triggering level at higher voltages than the neutron-irradiated samples since they have a higher acceptor removal than the neutron which leaves less of the gain layer available.
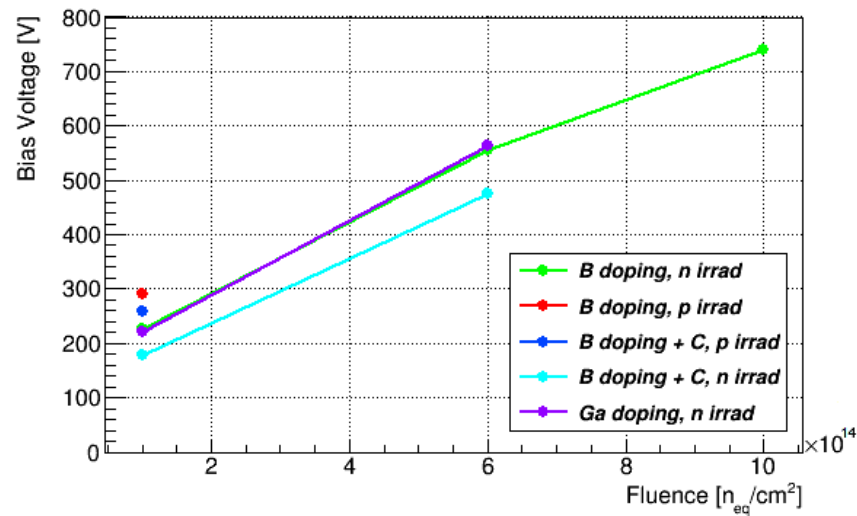
Figure 10. Maximum operating voltage for an auto-triggering rate of 1 kHz as a function of the fluence for CNM LGADs at $-30\,°C$.

6. Charged-Particle Measurements

6.1. Experimental Setup

The LGAD response to MIPs was characterized using 2 MeV electrons from a Sr-90 radiation source. Figure 11 illustrates the experimental setup. The encapsulated source is mounted on a 3D-printed support while the LGAD sensors are assembled on custom readout boards [25]. Two LGADs (one reference and the one being studied) are mounted back-to-back on an aluminum L-shaped support frame and aligned with respect to the source, which is also mounted in such a support frame. This system is operated inside a climate chamber (Votsch VT4002) at low temperatures (down to $-30\,°C$). Dry air is provided to the chamber ambient to avoid condensation on the sensor surface which could damage it. The bias voltage is supplied to each sensor with a sourcemeter (Keithley 2410 1100 V SourceMeter [18]). A low voltage supply (Rohde & Schwarz HMP4040 Programmable power supply 384 W [26]) provides the 2.25 V needed for the signal first amplification stage (on-board) and the 12 V needed for a second amplification stage (external). These instruments are connected to an oscilloscope (LeCroy Waverunner 8104 1 GHz Oscilloscope 20 GS/s [24]) that runs the acquisition software. The climate chamber is also connected to the oscilloscope via a local area network (LAN) with a fixed Internet protocol (IP). The LabVIEW-based automated interface that has been developed as a control software and that, in this setup, runs on the oscilloscope is described in Section 6.3. The output analog signals from the readout boards are recorded with the oscilloscope for every coincidence trigger between the two tested sensors. The data are saved for off-line waveform processing as it is explained in Section 6.4. Measurements are performed at $-30\,°C$ and at different bias voltages. A run corresponds to a voltage point.

6.2. Procedure

Initially, a boron unirradiated LGAD is calibrated with an identical sensor in the setup explained in Section 6.1. Both devices should have very similar properties such as the collected charge and the time resolution. In this way, the intrinsic performance before irradiation can be assessed. Afterwards, this boron unirradiated sample is used as time reference for testing the other set of LGADs, that we will call DUTs. The reference is operated at a fixed bias voltage, which was determined from the auto-triggering studies (80 V at $-30\,°C$). The DUTs are operated in a range of voltage in the stable region.
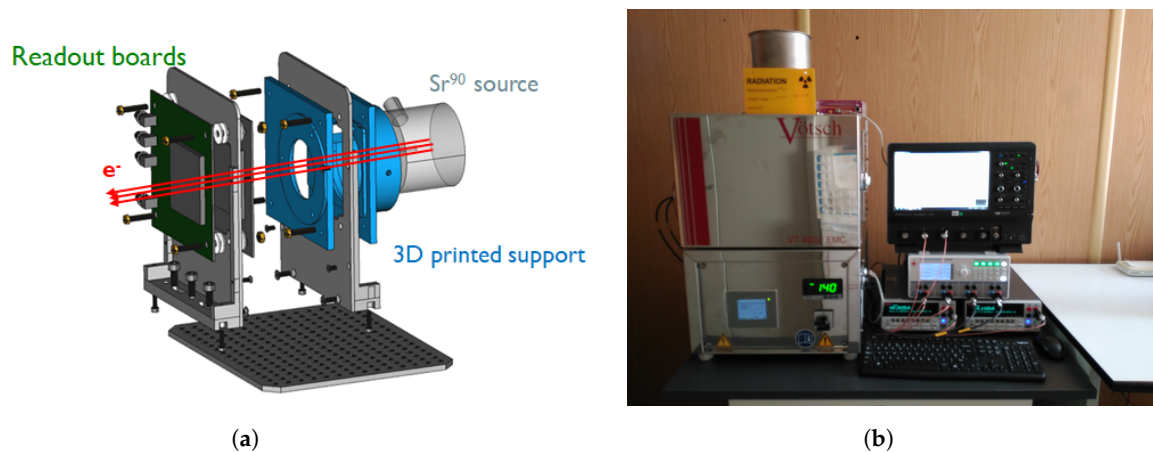
| (**a**) | (**b**) |

Figure 11. (**a**) Sketch and (**b**) photograph of the Sr-90 setup in the laboratory.

6.3. DAQ and Control System

The DAQ system described in Section 6.1 is controlled using a LabVIEW interface. This control software interface is organized in four tabs: (i) HV control, (ii) V-I recording and visualization as a function of time, (iii) low voltage control and (iv) temperature control and monitoring. Tabs i, iii and iv support multiple instruments through an adaptive polymorphic user interface. The interface also integrates error handling. The oscilloscope has its own software (DSO) for waveform display, trigger mode configuration and record data saving waveforms per trigger per active channel for these particular measurements.

6.4. Analysis Software

The data taken at the laboratory has been analyzed using a C++-based software framework, LGADUtils [27], which performs the oscilloscope data conversion, the waveform processing with a calculation of the signal properties and, in the case of test beam mode, also merges the oscilloscope and telescope data into a single ROOT ntuple [28].

The initial step of the analysis is to convert the oscilloscope ASCII data into a ROOT ntuple containing the raw waveform information. The second step is the waveform processing with a determination of the pulse polarity, the maximum and minimum of the signal and the signal start and stop points. With this information, it classifies the signal as noise or as a real signal event and checks if the complete pulse is within the oscilloscope acquisition time window. Once this is performed, the pedestal and noise are calculated in the 10-90% range before the start of the signal using a Gaussian fit and defined as the mean and the standard deviation of the fit, respectively. The pedestal is subtracted to the waveform, the pulse is inverted (in the case of negative polarity) and minimum, maximum, start and stop points are re-calculated. The third step is the computation of several waveform properties: collected charge, rise time, jitter, signal to noise ratio and Time Of Arrival (TOA) at different thresholds. The last step is the user analysis where timing and efficiency are calculated. As a result, after running LGADUtils, the final ntuple contains the raw waveform information and its properties.

6.5. Collected Charge

For each event in a run, the charge from the recorded waveform is calculated as the integral of the signal area. A charge distribution is plotted and fitted using a Landau–Gauss convoluted function where the collected charge is defined as the most probable value of the fitted function. Figure 12 shows the collected charge as a function of the bias voltage for sensors irradiated at different fluences up to 10^{15} n_{eq}/cm^2 at $-30\,°C$. Boron plus carbon sensors have a larger charge collection than boron and gallium sensors at a same bias voltage. In this aspect, carbon-enriched gain layers help to reduce the effect of gain reduction with irradiation. However, as seen in Section 5, carbon sensors from this initial

production run start auto-triggering earlier in voltage than boron and gallium ones, and it is not possible to operate them at higher voltages.
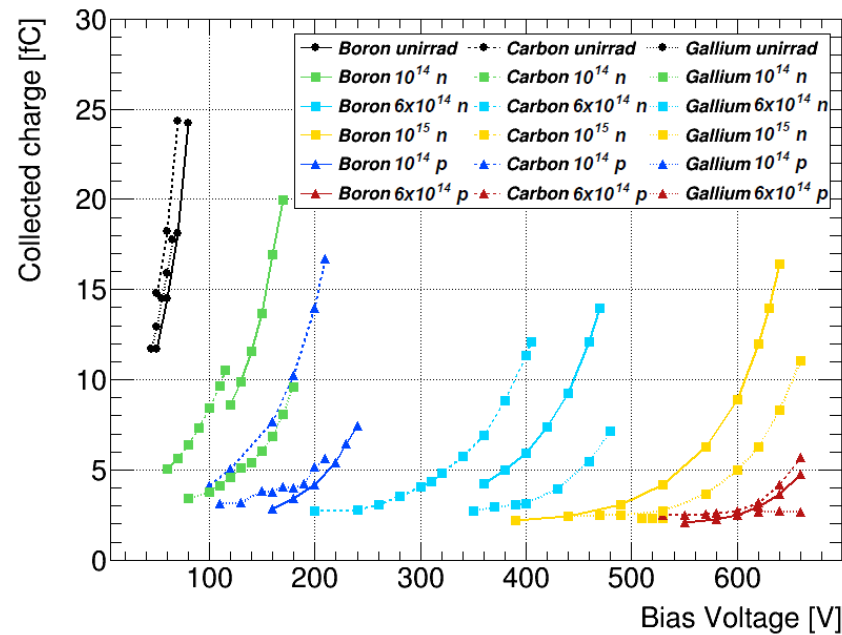

Figure 12. Collected charge as a function of the bias voltage for CNM LGADs irradiated up to a fluence of 10^{15} n_{eq}/cm^2 at $-30\,°C$.

6.6. Time Resolution

Similarly to the collected charge procedure, the software analysis tool allows us to determine, for each event in a run, the TOA of the recorded waveform as the time crossing a given threshold using the Constant Fraction Discriminator (CFD) method or the Time-Over-Threshold (TOT) technique. In what follows, the CFD method is used. The set threshold corresponds to a certain fraction, f_{CFD}, of the signal maximum in steps of 0.05. The time resolution is calculated from the distribution of the difference of the TOAs of the reference and the DUT LGADs as it is explained below. The optimal fraction from the CFD method, at which the signal is discriminated and, therefore, the TOA determined, is defined by the dominant contribution to the time resolution. In the case of an unirradiated sensor, the dominant contribution is the Landau term whereas for an irradiated sensor, the dominant effect is the jitter, therefore a higher threshold is required (see Figure A3). In the following subsection, the procedure for optimizing the timing is described. The aim is to find an optimal fraction achieving the best time resolution.

6.6.1. CFD Optimization

The timing performance of the unirradiated boron LGAD is evaluated first, using the procedure described above in Section 6.2. It was calibrated with an identical sensor and both are considered here as DUT_1 and DUT_2. The time difference between the TOA of DUT_1 and that of DUT_2 is calculated using all possible combinations of CFD fractions. A two-dimensional map of f_{CFD} for DUT_1 and DUT_2 is made and illustrated in Figure 13a. The z-axis corresponds to the time resolution defined as the σ from the Gaussian fit of the time difference distribution divided by $\sqrt{2}$. From this map, the CFD fraction achieving the minimum time resolution for the unirradiated boron LGAD is obtained and amounts to $f_{CFD} = 0.15$.

The timing resolution of the other LGADs (or DUTs) is then determined using the performance of the reference device. The time difference distributions between the TOA of the reference at the optimal CFD fraction of $f_{CFD} = 0.15$ and the TOA of the DUT at all CFD fractions are built and fitted with Gaussians. A histogram of the time resolution,

σ, as a function of f_{CFD} for the DUT is shown in Figure 13b. In the vertical axis, the time resolution is computed as:

$$\sigma_i = \sqrt{\sigma^2_{DUT_{f_{CFDi}}} - \sigma^2_{refLGAD_{f_{CFD=0.15}}}}, \tag{2}$$

The fraction that gives the minimum time resolution for the DUT is then obtained. For this specific DUT, unirradiated gallium LGAD operated at 60 V and at $-30\,°C$, the optimal CFD fraction was found to be $f_{CFD} = 0.2$, achieving a time resolution of 45.7 ps.

Using this optimization method, the time resolution was found to be better than 50 ps for sensors irradiated at fluences higher than 6×10^{14} n_{eq}/cm^2 at $-30\,°C$. Unirradiated sensors and sensors irradiated at a low fluence of 10^{14} n_{eq}/cm^2 feature a time resolution below 40 ps at their highest operating voltages. Figure 14 shows the time resolution as a function of the bias voltage for all of the sensors at $-30\,°C$, where the contribution from the reference sensor of 35.7 ps with $f_{CFD} = 0.15$ is already subtracted. The slope of the time resolution for the unirradiated sensors is steep due to the high gain. Boron and boron plus carbon sensors show similar performance, whereas gallium sensors achieve a larger time resolution due to the high leakage current.
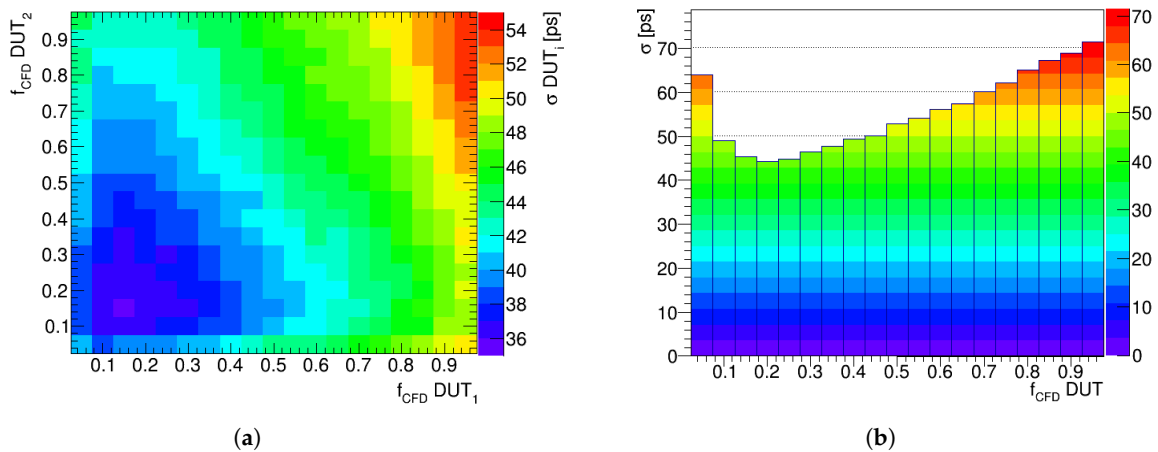

(**a**)   (**b**)

Figure 13. (**a**) Two-dimensional map of time resolution as a function of CFD fractions for unirradiated boron CNM LGADs. (**b**) Time resolution as a function of a CFD fraction for a DUT sensor (unirradiated gallium).
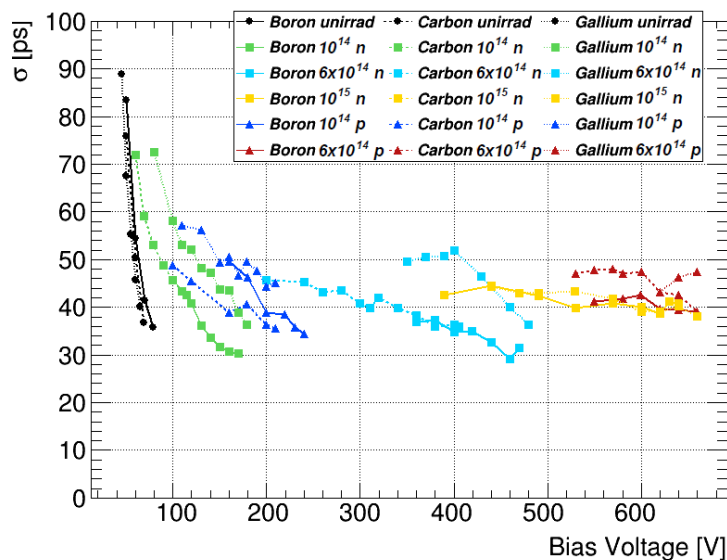

Figure 14. Time resolution as a function of bias voltage for CNM LGADs irradiated up to a fluence of 10^{15} n_{eq}/cm^2 at $-30\,°C$.

7. Conclusions and Outlook

Picosecond timing detectors are going to be used by the LHC experiments to cope with the high-multiplicity events during the coming high luminosity period where the timing information helps to assign tracks to the correct vertices, mitigating the effect of pile-up. The LGAD technology is a good candidate due to its excellent performance before irradiation, achieving a time resolution of about 30 ps. LGAD producers are targeting to deliver thin sensors providing good time resolution, fine segmentation and radiation hardness.

In this paper, the performance of CNM LGADs before and after irradiation up to fluences of 10^{15} n_{eq}/cm^2 has been presented. Different doping materials, boron and gallium, were investigated. Boron plus carbon sensors have a larger charge collection than boron and gallium at the same bias voltage. Carbon helps to diminish the effect of gain reduction with irradiation. Although, boron plus carbon sensors start auto-triggering earlier in voltage than the other two implants which makes them not operable at higher voltages. Thus, the determining factor for carbon is not radiation hardness but stability. However, later productions at different vendors have shown improved performance for carbonated sensors [29]. The key difference being that in this production, the carbon was introduced at the beginning of the run, and then is likely to have been diffused away from the multiplication layer. Gallium presents 20% less gain with respect to boron and achieves a worse time resolution due to the high leakage current. Gallium process instabilities require better diffusion techniques. This line of research has not been further pursued given the poorer radiation hardness and timing performances. The gain of boron and gallium samples was studied as a function of bias voltage using a TCT setup. Boron LGADs show more gain than the gallium ones at the same bias voltages and it is in agreement with the Sr-90 source results.

Nowadays, the interest is to study LGADs and their performance at high fluences beyond 10^{15} n_{eq}/cm^2. However, the performance remains challenging due to degradation of the gain layer. The latest runs by CNM from 2020 and 2021 have been produced with higher boron implant doses (1.8×10^{13} at/cm^2 and 2×10^{13} at/cm^2) on Si-on-Si and epitaxial wafers. The aim of these runs is to be able to operate the LGADs further in bias voltage. A full characterization of the samples from these runs before and after extreme fluences up 10^{16} n_{eq}/cm^2 is presented in [30]. A new run on epitaxial wafers with carbon implanted in the gain layer is under production.

Institutional Review Board Statement: Not applicable.

Informed Consent Statement: Not applicable.

Data Availability Statement: The code used in this work, which is in development and continuously updated, is publicly available and at https://gitlab.cern.ch/egkougko/lgadutils (accessed on 9 November 2021). The data presented in this study are available in article.

Conflicts of Interest: The authors declare no conflict of interest.

Abbreviations

The following abbreviations are used in this manuscript:

IFAE	Institut de Física d'Altes Energies
BIST	Barcelona Institute of Science and Technology
CERN	Conseil Européen pour la Recherche Nucléaire
CNM	Centro Nacional de Microelectrónica
LGAD	Low Gain Avalanche Detector
MIP	Minimum Ionizing Particle
HL-LHC	High-Luminosity Large Hadron Collider
HGTD	High-Granularity Timing Detector
ETL	End-cap Timing Layer
I-V	Current-Voltage
C-V	Capacitance-Voltage
TCT	Transient Current Technique
LHC	Large Hadron Collider
ITk	Inner Tracker
PV	Primary Vertex
JTE	Junction Termination Extension
SSD	Solid State Detectors
IR	Infra-Red
DUT	Device Under Test
DAQ	Data Acquisition
TOA	Time Of Arrival
CFD	Constant Fraction Discriminator
TOT	Time-Over-Threshold

Appendix A. Additional Results

Appendix A.1. I-V Curves at Room Temperature

Each device was pre-characterized at the producer site where current-voltage (I-V) measurements at room temperature were also performed, as shown in Figure A1.
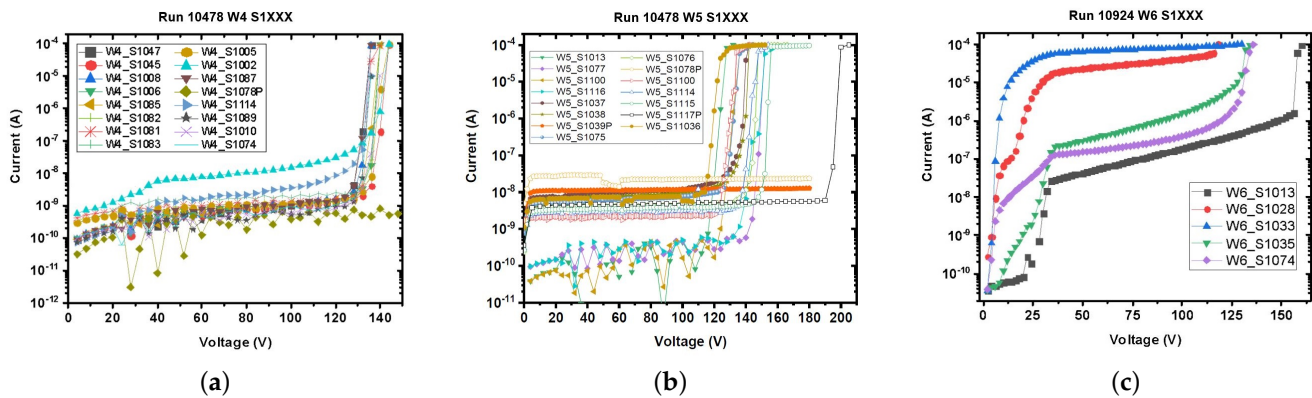

(**a**)　　　　　　　(**b**)　　　　　　　(**c**)

Figure A1. I-V characteristic curves for (**a**) boron, (**b**) boron plus carbon and (**c**) gallium LGADs performed at room temperature by CNM [12].

Appendix A.2. Time Resolution Behavior with Charge

After irradiation, the expected decrease of the gain can be mitigated by increasing the bias voltage. Figure A2 summarizes results obtained in the laboratory, with dedicated electronics for sensors exposed to fluence up to 10^{15} n_{eq}/cm^2. The performance of all sensors is similar.
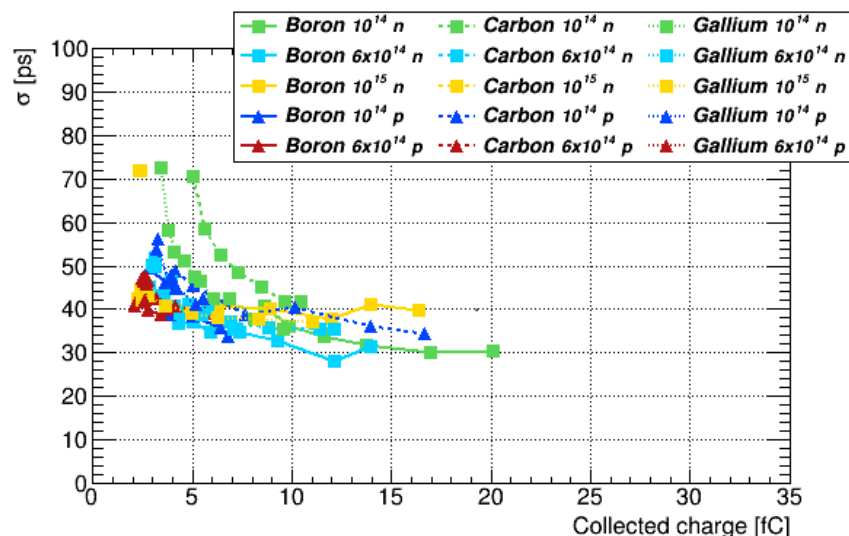
Figure A2. Time resolution as a function of the collected charge for CNM LGADs irradiated up to a fluence of 10^{15} n_{eq}/cm^2 at $-30\,°C$.

Appendix A.3. CFD Fraction Behavior with Fluence

The optimal f_{CFD} providing the best time resolution at each bias voltage point has been obtained, as explained in Section 6.6.1. Figure A3 shows the CFD fraction as a function of the bias voltage. Irradiated devices require higher f_{CFD} than unirradiated sensors as the dominant contribution is the jitter.
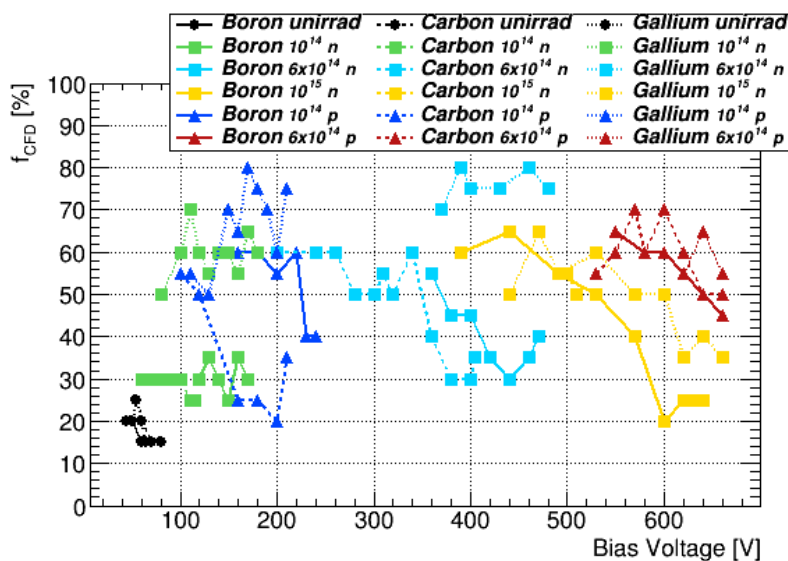

Figure A3. CFD fraction as a function of the bias voltage for CNM LGADs irradiated up to a fluence of 10^{15} n_{eq}/cm^2 at $-30\,°C$.

Appendix A.4. Other Signal Properties

In the paper, the most critical parameters of the sensors have been presented. However, from the recorded waveforms after offline analysis, other properties of interest have been calculated as mentioned in Section 6.4.

Appendix A.4.1. Noise

The noise in Figure A4 is calculated in the 10–90% range before the start of the signal and is defined as the σ of a Gaussian fit. For all of the sensors, the noise is below $2\,mV$.
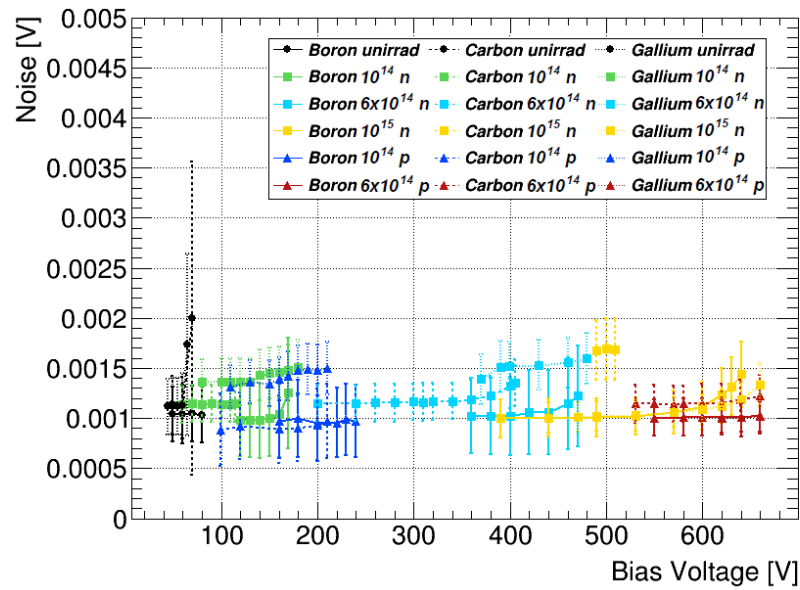
Figure A4. Noise as a function of the bias voltage for CNM LGADs irradiated up to a fluence of 10^{15} n_{eq}/cm^2 at $-30\,°C$. The error bars are determined from a Gaussian fit.

Appendix A.4.2. Rise Time

The rise time of the signal in Figure A5 is calculated as the time elapsed between the 10% of the amplitude to the 90%. Unirradiated sensors are slower within the range 0.6 ns to 1.1 ns. Irradiated sensors are then faster and have a rise time of 0.5 ns on average. Unirradiated sensors have a low drift field, whereas, at larger fluence, the increase at high bias is due to the delayed holes from the gain process [31].
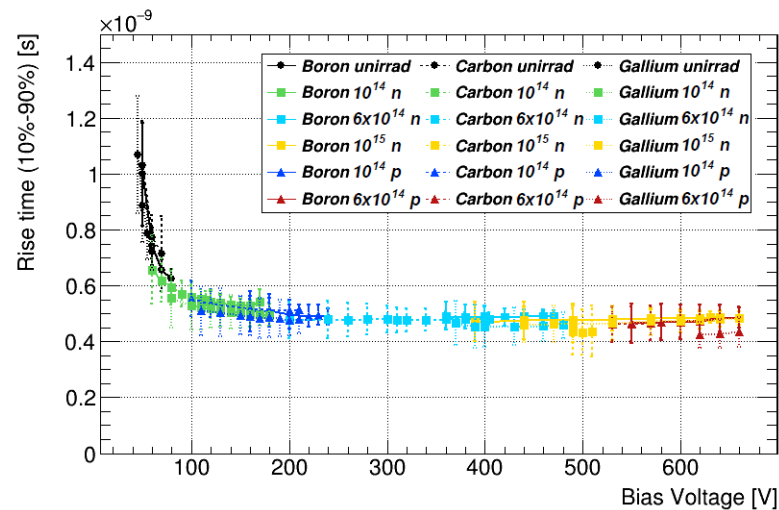
Figure A5. Rise time as a function of the bias voltage for CNM LGADs irradiated up to a fluence of 10^{15} n_{eq}/cm^2 at $-30\,°C$. The error bars are determined from a Gaussian fit.

Appendix A.4.3. Jitter

The jitter is an important contribution to the electronics noise and depends inversely on the signal slope dV/dt. The jitter in Figure A6 is calculated as:

$$\sigma_{jitter} = \frac{N}{dV/dt} \tag{A1}$$

where N is the electronics noise.

As expected, the jitter of all of the sensors becomes better with the increase of bias voltage. This is a consequence of a stronger electrical field in the sensor volume and a higher gain. Moreover, the velocity of carriers becomes saturated with higher bias, and the contribution of distortion to the time resolution is reduced [32].
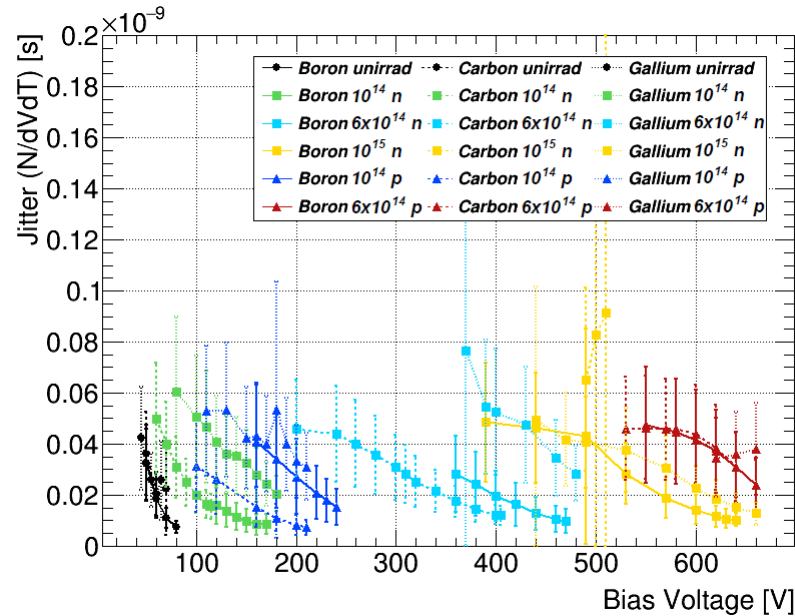

Figure A6. Jitter as a function of the bias voltage for CNM LGADs irradiated up to a fluence of 10^{15} n_{eq}/cm^2 at $-30\,°C$. The error bars are determined from propagation of uncertainty.

Appendix A.4.4. Signal-to-Noise Ratio

The signal-to-noise ratio is shown in Figure A7. At low fluences, boron and boron plus carbon sensors perform similarly. However, gallium has not demonstrated clear beneficial results, hence, it is not considered as a candidate for future productions.
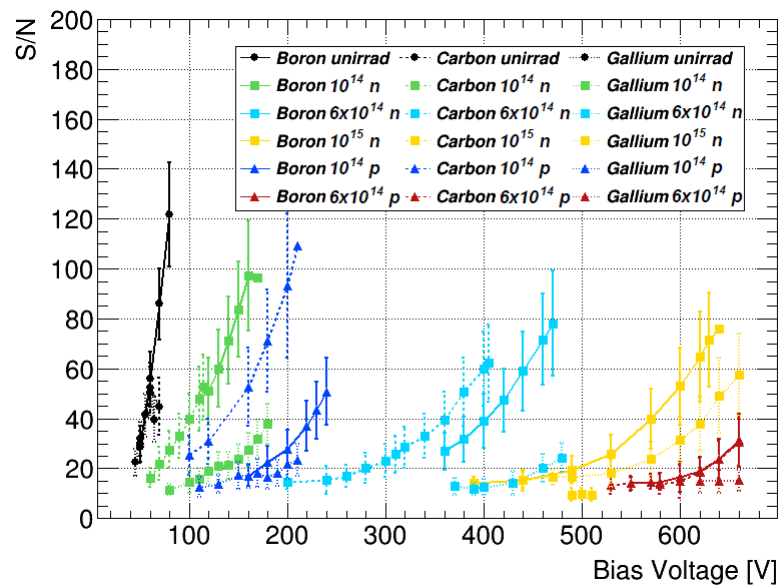

Figure A7. Signal-to-noise ratio as a function of the bias voltage for CNM LGADs irradiated up to a fluence of 10^{15} n_{eq}/cm^2 at $-30\,°C$. The error bars are determined from propagation of uncertainty.

References

1. Rossi, L.; Brüning, O. *High Luminosity Large Hadron Collider: A Description for the European Strategy Preparatory Group*; Technical Report CERN-ATS-2012-236; CERN: Geneva, Switzerland, 2012.
2. Apollinari, G.; Béjar Alonso, I.; Brüning, O.; Fessia, P.; Lamont, M.; Rossi, L.; Tavian, L. *High-Luminosity Large Hadron Collider (HL-LHC): Technical Design Report V. 0.1*; CERN Yellow Reports: Monographs; CERN: Geneva, Switzerland, 2017; [CrossRef]
3. The ATLAS Collaboration. The ATLAS Experiment at the CERN Large Hadron Collider. *J. Instrum.* **2008**, *3*, S08003. [CrossRef]
4. The CMS Collaboration. The CMS experiment at the CERN LHC. *J. Instrum.* **2008**, *3*, S08004. [CrossRef]
5. The ATLAS Collaboration. *Technical Design Report for the ATLAS Inner Tracker Pixel Detector*; Technical Report CERN-LHCC-2017-021, ATLAS-TDR-030; CERN: Geneva, Switzerland, 2017.
6. Sadrozinski, H.F.W.; Seiden, A.; Cartiglia, N. 4-Dimensional Tracking with Ultra-Fast Silicon Detectors. *arXiv* **2017**, arXiv:1704.08666.
7. Pellegrini, G.; Fernández-Martínez, P.; Baselga, M.; Fleta, C.; Flores, D.; Greco, V.; Hidalgo, S.; Mandić, I.; Kramberger, G.; Quirion, D.; et al. Technology developments and first measurements of Low Gain Avalanche Detectors (LGAD) for high energy physics applications. *Nucl. Instrum. Methods Phys. Res. Sect. A Accel. Spectrometers, Detect. Assoc. Equip.* **2014**, *765*, 12–16. [CrossRef]
8. The ATLAS Collaboration. *Technical Proposal: A High-Granularity Timing Detector for the ATLAS Phase-II Upgrade*; Technical Report CERN-LHCC-2018-023. LHCC-P-012; CERN: Geneva, Switzerland, 2018.
9. The CMS Collaboration. *Technical Proposal for A MIP Timing Detector in the CMS Experiment Phase 2 Upgrade*; Technical Report CERN-LHCC-2017-027. LHCC-P-009; CERN: Geneva, Switzerland, 2017.
10. Williams, M. The LHCb VELO Upgrade II. In Proceedings of the International Workshop on Semiconductor Pixel Detectors for Particles and Imaging (PIXEL2018), Taipei, Taiwan, 10–14 December 2018. Available online: https://indico.cern.ch/event/669866/contributions/3235374/ (accessed on 25 December 2021).
11. Pellegrini, G.; Carulla, M.; Flores, D.; Hidalgo, S.; Quirion, D. Status of LGAD productions at CNM. In Proceedings of the 30th RD50 Workshop, Krakow, Poland, 5–7 June 2017. Available online: https://indico.cern.ch/event/637212/contributions/2608652/ (accessed on 25 December 2021).
12. Hidalgo, S.; Carulla, M.; Doblas, A.; Flores, D.; Merlos, A.; Pellegrini, G.; Quirion, D. CNM activities on LGADs for ATLAS/CMS Timing Layers. In Proceedings of the 32th RD50 Workshop, Hamburg, Germany, 4–6 June 2018. Available online: https://indico.cern.ch/event/719814/contributions/3022492/ (accessed on 25 December 2021).
13. Carulla, M. *Thin LGAD Timing Detectors for the ATLAS Experiment*; Universitat Autonoma de Barcelona, Barcelona, Spain, 2019. Available online: https://www.tesisenred.net/handle/10803/667283#page=1 (accessed on 25 December 2021).
14. Lange, J.; Carulla, M.; Cavallaro, E.; Chytka, L.; Davis, P.; Flores, D.; Förster, F.; Grinstein, S.; Hidalgo, S.; Komarek, T.; et al. Gain and time resolution of 45 μm thin Low Gain Avalanche Detectors before and after irradiation up to a fluence of 1015 n_{eq}/cm^2. *J. Instrum.* **2017**, *12*, P05003. [CrossRef]
15. Cavallaro, E. *Novel Silicon Detector Technologies for the HL-LHC ATLAS Upgrade*; Universitat Autonoma de Barcelona, Barcelona, Spain, 2018. Available online: https://www.tesisenred.net/handle/10803/666621#page=1 (accessed on 25 December 2021).
16. Allaire, C.; Benitez, J.; Bomben, M.; Calderini, G.; Carulla, M.; Cavallaro, E.; Falou, A.; Flores, D.; Freeman, P.; Galloway, Z.; et al. Beam test measurements of Low Gain Avalanche Detector single pads and arrays for the ATLAS High Granularity Timing Detector. *J. Instrum.* **2018**, *13*, P06017. [CrossRef]
17. The RD50 Collaboration. Available online: https://rd50.web.cern.ch/rd50 (accessed on 25 December 2021).
18. 2410 Sourcemeter Datasheet. Available online: https://www.tek.com/en/sitewide-content/datasheets/s/e/r/series-2400-sourcemeter-instruments (accessed on 25 December 2021).
19. Gkougkousis, E.L.; Garcia, L.C.; Grinstein, S.; Coco, V. Comprehensive technology study of radiation hard LGADs. *arXiv* **2021**, arXiv:2111.06731.
20. Gkougkousis, E.L.; Castillo García, L.; Coco, V. A comparative study of LGAD radiation damage mechanisms. In Proceedings of the Workshop on Pico-Second Timing Detectors for Physics, Zurich, Switzerland, 9–11 September 2021. Available online: https://indico.cern.ch/event/861104/contributions/4514659/ (accessed on 25 December 2021).
21. Kramberger, G. Advanced Transient Current Technique Systems. In Proceedings of the 23rd International Workshop on Vertex Detectors (Vertex 2014), Doksy, Czech Republic, 15–19 September 2014.
22. Simon Argemi, L.; Grinstein, S.; Lange, J. TCT Measurements on 3D Small Pitch Strip Detectors, 2016. Master's Thesis, Universitat Autonoma de Barcelona, Barcelona, Spain, 2016.
23. Ritt F, S.; Dinapoli, R.; Hartmann, J. Application of the DRS Chip for Fast Waveform Digitizing. *Nucl. Instrum. Methods Phys. Res. A* **2010**, *623*, 486–488. [CrossRef]
24. Lecroy 8000 Datasheet. Available online: http://cdn.teledynelecroy.com/files/pdf/waverunner8000-datasheet.pdf (accessed on 25 December 2021).
25. Galloway, Z.; Fadeyev, V.; Freeman, P.; Gkougkousis, E.; Gruey, B.; Labitan, C.A.; Luce, Z.; McKinney-Martinez, F.; Sadrozinski, H.F.W.; Seiden, A.; et al. Properties of HPK UFSD after neutron irradiation up to 6e15 n/cm^2. *arXiv* **2017**, arXiv:1707.04961.
26. Rohde & Schwarz Hmp Power Supplies User MANUAL. Available online: https://scdn.rohde-schwarz.com/ur/pws/dl_downloads/dl_common_library/dl_manuals/gb_1/h/hmp_serie/HMPSeries_UserManual_en_02.pdf (accessed on 25 December 2021).

27. LGADUtils: A C++ Based Framework for Waveform Analysis. Available online: https://gitlab.cern.ch/egkougko/lgadutils (accessed on 25 December 2021).

28. Castillo García, L. A High-Granularity Timing Detector for the Phase-II upgrade of the ATLAS Calorimeter system: detector concept, description and R&D and beam test results. *J. Instrum.* **2020**, *15*, C09047.

29. Kramberger, G. *LGADs for Timing Detectors at HL-LHC*; Jožef Stefan Institute: Ljubljana, Slovenia, 2021. Available online: https://indico.cern.ch/event/1088953/ (accessed on 25 December 2021).

30. Grieco, C. Overview of CNM LGAD results: Boron Si-on-Si and epitaxial wafers. In Proceedings of the 12th International Conference on Position Sensitive Detectors, Birmingham, UK, 12–17 September, 2021.

31. Sadrozinski, H. Timing Resolution Measurements on Utra-fast Silicon Detectors. In Proceedings of the International 'Hiroshima' Symposium on the Development and Application of Semiconductor Tracking Detectors (HSTD-11), Okinawa, Japan, 10–15 December 2017. Available online: https://indico.cern.ch/event/577879/contributions/2740418/ (accessed on 25 December 2021).

32. Lastovicka-Medin, G.; Andreasson, J.; Cartiglia, N.; Černý, J.; Kramberger, G.; Kroll, J.; Kropielniczki, K.; Lastovicka, T.; Rebarz, M.; Sola, V.; et al. First LGAD timing/jitter measurement at ELI with fs-lasers of 800 nm and 1450 nm. In Proceedings of the 36th RD50 Workshop, Zurich, Switzerland, 3–5 June 2020. Available online: https://indico.cern.ch/event/918298/contributions/3880602/ (accessed on 25 December 2021).